**AlPO4-5 zeolite at high pressure: crystal-fluid interaction and elastic behavior**

(Article begins on next page)

28 July 2024

# AlPO$_4$-5 zeolite at high pressure:

# crystal-fluid interaction and elastic behavior.

Paolo Lotti[a*†], G. Diego Gatta[a,b], Davide Comboni[a], Marco Merlini[a], Linda Pastero[c], Michael Hanfland[d]

[a] Dipartimento di Scienze della Terra, Università degli Studi di Milano, Via Botticelli 23, 20133 Milano, Italy

[b] CNR – Istituto di Cristallografia, Sede di Bari, Via G. Amendola 122/O, Bari, Italy

[c] Dipartimento di Scienze della Terra, Università degli Studi di Torino, Via Valperga Caluso 35, 10135 Torino, Italy

[d] ESRF – European Synchrotron Radiation Facility, 71 Avenue des Martyrs, CS40220, 38043 Grenoble Cedex, France.

\* Corresponding Author:

Phone: +39-0403758735; e-mail: paolo.lotti@elettra.eu

[†] Present address: Elettra Sincrotrone Trieste S.c.P.A., Strada Statale 14, km. 163.5, 34149 Basovizza, Trieste, Italy.

**Abstract**

The high-pressure behavior of the aluminophosphate zeolite $AlPO_4$-5 (AFI-topology) has been investigated by *in situ* single-crystal synchrotron X-ray diffraction with a diamond anvil cell, using the "non-penetrating" silicone oil and the "penetrating" 16:3:1 methanol:ethanol:water (*m.e.w.*) mixture as *P*-transmitting fluids. The crystals used in this study showed diffraction patterns typical of an incommensurate modulated structure, with modulation vector $q \approx 0.37\mathbf{c^*}$. Compression in silicone oil showed that $AlPO_4$-5 is one of the softest zeolites reported so far, being its refined bulk modulus ($K_{V0} = 1/\beta_V$) at ambient conditions only 13.2(11) GPa ($\beta_V = 0.076(6)$ GPa$^{-1}$), with an elastic anisotropy $K_a:K_c = 1.6$. The high-pressure experiment performed using *m.e.w.* showed a significantly lower compressibility of $AlPO_4$-5, if compared to the behavior in silicone oil, suggesting the occurrence of a *P*-induced intrusion of the fluid molecules into the zeolitic cavities. An indirect evidence for the molecules intrusion is provided by the comparative analysis of the structure deformation mechanisms at the atomic scale. When zeolite $AlPO_4$-5 is compressed in *m.e.w.*, a lower degree of distortion of the secondary building units is observed, with respect to the compression in silicone oil. Overall, this study suggests zeolite $AlPO_4$-5 as a promising microporous material for the pressure-mediated intrusion and hyper-confinement of molecules into the structural micropores.

## 1. Introduction

Aluminophosphate $(Al,P)_nO_{2n}$ compounds [1–2] are a group of microporous materials, which share with the most common $(Al,Si)_nO_{2n}$ zeolites a large diversity of structures [2–3], as well as applications as molecular sieves, catalysts, etc. [1]. An important member of this group is the aluminophosphate zeolite number 5 ($AlPO_4$-5, [4]), with the AFI-framework type [5]. As shown by the high number of very recent studies, spanning from synthesis methods (e.g. [6–7]) to structural characterization (e.g. [8]) or potential technological and industrial applications (e.g. [9–11]), $AlPO_4$-5 is an object of a growing research interest. The AFI-framework is characterized by very large channels made by 12-membered rings of tetrahedra (hereafter 12R-channels, Figure 1a), which are an ideal host for several molecules and polymers, as single-walled carbon nanotubes [11–13], dye molecules [14–15] or 1D-arrays of iodine [16], nitrogen [17], etc.

The AFI-framework shows a $P6/mcc$ topological symmetry, with ideal cell parameters $a$ = 13.827 and $c$ = 8.580 Å [5]. The 12R-channels are parallel to the [001] direction and centered to the six-fold axis (Figure 1a). Their largest free diameter (7.42 Å, [5]) is defined by the two symmetry-independent O1−O1 and O3−O3 (Figure 1a) interatomic distances. The channels are connected to each other by "pseudo-cage" cavities that are confined in the (001) plane by single 6-membered rings of tetrahedra centered on the 3-fold axis (hereafter S6R[001], Figure 1a). The access between the channels and these pseudo-cages is controlled by single 6-membered rings of tetrahedra, approximately parallel to the **c**-axis (hereafter S6R[$hk$0]$_1$, Figure 2a,c). However, in order to diffuse from a channel to the neighboring ones, a molecule/ion needs to cross a second symmetry-independent single 6-membered ring of tetrahedra (S6R[$hk$0]$_2$, Figure 2a,c). The diameters of these "windows" define the largest diameter of a sphere able to diffuse from a channel to another, reported to be 2.22 Å for the ideal AFI-framework [5].

The structure of $AlPO_4$-5 can also be described by the alternation, along the **c**-axis, of sheets made by isolated upward $AlO_4$ and downward $PO_4$ tetrahedra, respectively (Figure 1b). The $AlO_4$ and $PO_4$ tetrahedra bases are linked through the O1, O3 and O4 sites, whereas the O2 site acts as a bridge between the tetrahedra pointing upward and downward, respectively (Figure 2b). The observed distribution of Al and P between the tetrahedral sites reduces the symmetry of $AlPO_4$-5 from *P6/mcc* to *P6cc*. However, conflicting results are reported in the literature concerning the real symmetry of $AlPO_4$-5, as the space group *P6cc* leads to Al-O2-P interatomic angles close to 180°. A comprehensive overview is reported by Bordat et al. [18]. Several authors reported diffraction patterns being inconsistent with *P6cc,* and suggested the reduction of the $AlPO_4$-5 symmetry to a different hexagonal [19] or orthorhombic [20–22] subgroup of *P6cc*. Uncertainties concerning the real symmetry of $AlPO_4$-5 persist also if theoretical calculations are considered [18,23–24]. Therefore, a clear and unambiguous picture of the zeolite $AlPO_4$-5 crystal structure is still missing (see e.g. [8,19,25–26]). A more detailed discussion on this topic will be given in section 5.1.

In this study, we report, to the best of our knowledge for the first time in $AlPO_4$-5, the evidence for an incommensurate structural modulation analogous to that reported by Liu et al. [26] for zeolite SSZ-24. In addition, we investigate, by *in situ* single-crystal synchrotron X-ray diffraction, the high-pressure behavior of the zeolite $AlPO_4$-5 compressed in *"non-penetrating"* silicone oil and in *"penetrating"* (see e.g. [27]) methanol:ethanol:water (16:3:1) mixture (hereafter *m.e.w.*). The compression in silicone oil allows a description of the elastic behavior and of the general mechanisms of structure deformation (of the average *P6cc* structure), when no interference from the *P*-transmitting fluid occurs. On the other hand, the compression in the penetrating *m.e.w.* allows the study of the *P*-induced intrusion of fluid molecules into the structural cavities

of the zeolite $AlPO_4$-5, as well as the influence that this phenomenon plays on the elastic and structural response. The study of the high-pressure behavior of $AlPO_4$-5 is not a novelty, but a comprehensive characterization, especially of the mechanisms of structure deformation, is still missing. Lv et al. [17] investigated the high-pressure behavior of $AlPO_4$-5 compressed in silicone oil and in a mixture of silicone oil and liquid nitrogen, by synchrotron X-ray powder diffraction, and suggested a *P*-induced intrusion of nitrogen molecules. In addition, based on a splitting of diffraction peaks, the authors proposed the co-existence of hexagonal and orthorhombic phases at $P > 1.3$ GPa, but no structure refinements were performed. Kim et al. [28] studied the high-pressure behavior of $AlPO_4$-5, compressed in *m.e.w.*, by *in situ* synchrotron X-ray powder diffraction. These authors reported the occurrence of *P*-induced intrusion of fluid molecules in the range 0.0001−0.7 GPa and provided a description of the elastic behavior of $AlPO_4$-5, following the molecules intrusion. In this study, we confirm the *P*-induced penetration of the *m.e.w.* molecules into the $AlPO_4$-5 structural cavities and provide a description of the general mechanisms of structure deformation at the atomic scale, with or without the intrusion of fluid molecules. In addition, a discussion on the role played by the sample size (30-40 μm-sized single crystal *vs.* powders) on the high-*P* penetrability of fluid molecules is carried out.

This work is part of a research project on the crystal-fluid interaction at high pressure in microporous materials, and on its implications on the elasticity, structural deformation at the atomic scale and technological utilization of zeolites [29−34].

## 2. Experimental methods

The synthesis routine of the sample of AlPO$_4$-5 used in this study was modified from the one proposed by Li et al. [35]. The molar composition of the synthesis gel was modified as follows:

1Al$_2$O$_3$ : 1.33P$_2$O$_5$ : 0.6TEA : 100H$_2$O
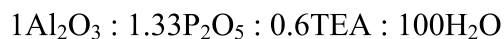
Aluminum isopropoxide, phosphoric acid and triethylamine were all Sigma analytical grade reagents. Ultrapure water 18 MOhm was obtained using an Elga Flex3 water purification system.

Aluminum isopropoxide and water were mixed on the basis of the molar ratios previously indicated and stirred for 4 hours. Phosphoric acid was added and the suspension was stirred further for 1 hour. TEA was then added and stirred vigorously for 10 minutes. The synthesis gel was kept at room temperature for 12 hours and afterwards it was heated at 210 °C for 4 days. The synthesis product was filtered, washed with ultrapure water and dried at room temperature. The as-synthesized sample was then calcined up to 600°C, in order to completely remove the template molecules from the zeolitic cavities.

A thermogravimetric analysis of the calcined sample was carried out using a Seiko SSC 5200 thermal analyzer. The sample was loaded in a Pt crucible and heated in an air flux (100 mL/min) from room temperature up to 880 °C (increment rate, 10 °C/min).

Single crystals showing hexagonal prismatic morphology (ca. 20·20·40 μm$^3$ in size) were selected for the diffraction experiments performed at the ID09A beamline of the European Synchrotron Radiation Facility (ESRF) in Grenoble, France. A parallel monochromatic beam ($E$ = 30 KeV, $\lambda$ = 0.414 Å) was used; the diffraction patterns were collected by a MAR555 flat-panel detector, positioned at 287.43 mm from the sample position. Further details on the beamline experimental setup are reported in

Merlini and Hanfland [36]. A first data collection was performed with a crystal in air mounted on a glass fiber. A stepwise ω-rotation in the range ± 45°, with 1° step width and 1s exposure time per step, was adopted as collection strategy. Two high-pressure experiments were then performed using silicone oil and a 16:3:1 = methanol:ethanol:water mixture (*m.e.w.*, [37]) as *P*-transmitting fluids, respectively. $H_2O$, methanol and ethanol molecules (kinetic diameters 2.65, 3.76 and 4.46 Å, respectively) can potentially be incorporated into the large 12-ring channels of $AlPO_4$-5 (∅ = 7.3 Å, [5]). For both the *P*-experiments, membrane-driven diamond anvil cells (DACs), mounting Boehler-Almax designed diamonds (culet diameter 600 μm), were used. Two selected crystals of $AlPO_4$-5 (one for each H*P*-experiment) were loaded in *P*-chambers obtained drilling a hole (∅ = 250 μm), by spark erosion, in a T301 stainless steel foil, previously pre-indented to ca. 70 μm and used as a gasket. Along with the zeolite crystals, the *P*-chambers were filled with the *P*-fluids and a few ruby chips as pressure calibrants (pressure uncertainty ± 0.05 GPa [38–39]). At any pressure point of both the ramps, the following data collection strategy was adopted: a stepwise ω-rotation of the DAC between -30 and +30°, with 1° step width and 1s exposure time per step. Unit-cell parameters were refined, from any dataset, by least-squares minimizations based on the positons of selected diffraction peaks using the *UnitCell* software [40] and are reported in Table 1. Intensity data reduction was performed using the *Crysalis* software [41], applying corrections for the background and the absorption of the DAC components adopting the implemented semi-empirical *ABSPACK* routine. Further details concerning the experimental datasets are reported in Table S1 (supplementary material).

## 3. Structure refinements

The crystals used in this study all show diffraction patterns typical of incommensurately modulated structures, with modulation vector $q \approx 0.37\mathbf{c}^*$ (Figure 3). However, the low intensity [$I \leq 3$ sig($I$)] of the satellite reflections did not allow the refinement of the incommensurate structure. More details and a discussion on this point are given in section 5.1.

The structure refinements were performed in the average space group $P6cc$ using the *JANA2006* software [42]. In addition to the structural complexity of AlPO$_4$-5, as reported in the section 1, and to the interference due to the DAC components on the intensity data, a sudden decrease of the $I$/sig($I$) ratio of the diffraction peaks was observed in all datasets for $d_{hkl} < 1$ Å, leading to a low number of "observed" reflections. For these reasons, a "*conventional*" refinement strategy was not possible, as will be described in the following paragraphs.

Fractional coordinates of the framework sites in the average space group $P6cc$ (unit cell parameters $a = 13.7175(12)$ and $c = 8.4350(8)$ Å) were obtained using the *SUPERFLIP* program [43], implemented in *JANA2006*. For the intensity data collected with the crystal in air, the position and the anisotropic displacement parameters of the framework sites were refined. The Al-O and the P-O distances were restrained to 1.74($\pm$0.02) and 1.52($\pm$0.02) Å, respectively. As expected, large anisotropic displacement parameters were obtained for all the sites. In particular, an elongated prolate shape, more or less parallel to $\mathbf{c}$, was obtained for the O1, O3 and O4 sites, whereas a flattened [in the (001) plane] oblate shape was obtained for the O2 site connecting the AlO$_4$ and PO$_4$ tetrahedra (Figure 2b), in fair agreement with the results of Klap et al. [19]. These large displacement parameters reflect a static (or dynamic) disorder, likely induced by the presence of rigid-unit modes or structural microdomains (see section 5.1), which in turn can lead to the sudden decrease in $I$/sig($I$) at high diffraction angles. Difference-Fourier

8

maps of the electron density were calculated, in order to locate the channel (water) population. However, in place of well defined residual peaks, a rather diffuse distribution of the electron density was found in a few specific portions of the 12R-channel and in the pseudo-cage close to the trigonal axis. Five oxygen sites were assigned to model the extraframework population and their coordinates and occupancies were refined assuming a reasonably high isotropic displacement parameter ($U_{iso} = 0.08$ Å$^2$), considering the disordered distribution of the residual peaks. Such a model necessarily implies that the refined positions and occupancies (biased by the assumed $U_{iso}$'s) of the channel $H_2O$-oxygens have to be considered mainly as a qualitative, rather than quantitative, structural information. A discussion on this point will be given in the section 5.1.

The same strategy described above was applied to refine the structure models based on the high-pressure intensity data. In this case, the independent refinement of the anisotropic displacement parameters of the framework sites was not possible for the lower number of the observed reflections (Table S1) and for the overall lower quality of the diffraction data, if compared to the collection with the crystal in air. Usually, in these conditions, isotropic displacement parameters are refined, in order to reduce the number of variables. However, in this specific case, constraining a large and highly anisotropic (Figure 2b) displacement to a spherical distribution of electron density decreased significantly the figure of merit of the refinement. Therefore, we have applied a *non-conventional* strategy that, on the other hand, we believe led to a refined model more closely related to the real structure: the anisotropic displacement parameters of the framework sites were refined, not simultaneously, in successive cycles, while all the atomic coordinates and the $H_2O$-oxygen occupancies were always refined. Although not conventional, compared to an isotropic refinement, this strategy allowed the decrease of

9

the $R_1$ factors of the refinements. The structure refinements were possible for the datasets up to 1.43 ($P_7$) and 2.44 ($P_9$) GPa in silicone oil and *m.e.w.*, respectively. At higher pressures, the low number of observed reflections did not allow reliable refinements. Further details on the structure refinements, refined site coordinates, occupancies and displacement parameters are deposited in Tables S1, S2 and S3 (supplementary materials). Relevant interatomic distances and structural parameters are reported in Table 2. A discussion of the refined structure models is in the section 5.1.

## 4. Results

### *4.1 Thermogravimetric analysis*

The thermogravimetric analysis of the calcined $AlPO_4$-5 sample shows a total weight loss of 18.35% at 880 °C (Figure 4). If we assume the loss as completely due to zeolitic $H_2O$ (adsorbed by the sample from the atmosphere after calcination, see section 5.1), the chemical formula of our (post-calcination) $AlPO_4$-5 sample is $AlPO_4 \cdot 1.52H_2O$, *i.e.* with 18.24 $H_2O$ molecules per unit cell, in fair agreement with previous TG-findings (e.g. [28,44]) and isotherm adsorption experiments (e.g. [45–46]). The TG- and DTG-data show that the dehydration mainly occurs in a single step (Figure 4), in the range 50-100 °C, with the maximum of the DTG at 85 °C.

### *4.2 High-pressure elastic behavior*

For the high-$P$ experiment in silicone oil, diffraction data at fourteen $P$-points up to 2.97 GPa, along with one point in decompression at 1.43 GPa, were collected. The intensity of the Bragg reflections decreased with increasing pressure to the extent that a reliable refinement of the unit-cell parameters was possible only up to 1.65 GPa (*i.e.* $P_8$). Intensities in the diffraction pattern were not recovered in decompression, suggesting that the average long-range order of the crystal was irreversibly lost by compression.

10

Seventeen $P$-points up to 6.51 GPa, with two points in decompression at 0.82 and 0.75 GPa, were collected for the ramp in $m.e.w.$. Although a decrease in the intensity of the diffraction peaks was observed with increasing pressure, the refinement of the unit-cell parameters was possible for all the datasets.

The $P$-induced evolution of the unit-cell parameters of $AlPO_4$-5 compressed in silicone oil and $m.e.w.$ are reported in Table 1 and shown in Figure 5. The compression in silicone oil leads to a monotonic decrease in $a$, $c$ and $V$, with no evidence of phase transitions or change in the compressional behavior. Due to the non-penetrating nature of silicone oil, the actual compressibility of $AlPO_4$-5 can be extrapolated from the related experimental data. A Birch-Murnaghan equation of state truncated to the third order (III-BM EoS, [47]) was fitted to the experimental $V$-$P$ data (Figure 5a) using the $EoSFit\ 7.0$ software [48], leading to the refined parameters reported in Table 3. The linear elastic behavior along the **a** and **c** crystallographic axes was also described by the fit of linearized BM-EoS [47]. However, in this case the refinement of three variables (namely: $l_0$, $K_{l0}$ and $K_l'$) was unstable. Therefore, $K_l' = \partial K_l/\partial P$ was fixed to the value that provided the best figure of merit. For the **a**-axis the best fit was obtained with $K_a' = 4$, whereas for the **c**-axis the best figure of merit was obtained with $K_c' = 7$. The other refined elastic parameters are reported in Table 3.

The $P$-induced evolution of the unit-cell parameters of $AlPO_4$-5 compressed in $m.e.w.$ shows an elongation of the structure along the **c**-axis between room-$P$ and 0.18 GPa, which is also reflected by a subtle change in the $V$-$P$ data slope (Figure 5a,d, Table 1). In addition, the comparison between the silicone oil and $m.e.w.$ data (Figure 5a) shows that $AlPO_4$-5 is significantly less compressible in the methanol:ethanol:water mixture. The potential penetration of $m.e.w.$ fluid molecules into the zeolitic cavities will be discussed in section 5.2. Apparently, neither discontinuities, nor changes in the

11

compressional behavior, are observed between 0.18 GPa ($P_1$) and the highest investigated pressure, *i.e.* 6.51 GPa ($P_{14}$). III-BM equations of state [47] were fitted to the experimental *V-P*, *a-P* and *c-P* data in the range $P_1$-$P_{14}$ (0.18-6.51 GPa, Figure 5a,c,d), leading to the refined elastic parameters reported in Table 3. The unit-cell parameters refined from the data collected in decompression at 0.82 ($P_{15d}$) and 0.75 ($P_{16d}$) GPa (Table 1) reveal that the bulk compression is not fully recovered at these pressures.

### 4.3 High-pressure structure evolution

#### 4.3.1 P-ramp in silicone oil

The structure refinements performed in space group *P6cc* allow a description of the *P*-induced deformation of the AlPO$_4$-5 average structure. As usually observed for open-framework materials (*e.g.* [27,49–50]), the bulk compression is accommodated by the tilting of the rigid (framework) tetrahedra, which leads to a compression of the structural cavities. To describe the framework deformation in our AlPO$_4$-5 structure, two geometrical models were arbitrarily defined for the large 12R-channels and the pseudo-cage cavities centered on the 3-fold axis (Figure 1a, 2a). The 12R-channel was modeled as a cylinder with height equal to the **c** unit-cell axis and base diameter D = (O1–O1 + O3–O3)/2, where O1–O1 and O3–O3 are the independent 12R-channel diameters (see Figure 1a). The pseudo-cage was modeled as a prism of height equal to the *c*-edge and triangular basis of side O4–O4 (see Figure 1a). The *V* vs. *P* evolution of the so-modelled 12R-channel and pseudo-cage is reported in Table 2 and shown in Figure 6a,b, where it can be seen that the compressibility of the pseudo-cage increases with pressure.

The tilting of the framework tetrahedra can be described by the deformation of the secondary building units of the AFI-framework. The 4-membered rings undergo a compression along both the O3–O3 and O4–O4 diameters (Figure 1a, Table 2) and a distortion from the (001) plane, as evidenced by the increasing deviation from the planarity, here described as $\Delta z_{4R} = (|(zO3 - 0.5) - zO4| \times c)$ (Table 2). Similarly, the distortion from the (001) plane of the S6R[001] is reflected by the increasing deviation from the planarity $\Delta z_{S6R[001]} = (|zO1 - zO4| \times c)$ reported in Table 2. The two symmetry-independent S6R[$hk0$]$_{1,2}$ windows are clearly distorted with increasing pressure (Figure 7), as shown by the increasing deformation parameters $\varepsilon_1$ and $\varepsilon_2$, defined as the ratio between the window diagonals (Figure 2a,c, Table 2).

As reported in the section 3, the refined coordinates of the extraframework $H_2O$ sites must be treated as an average position of a likely locally-disordered distribution, whereas the refined occupancies are biased by the constrained displacement parameters. Although with relevant uncertainty, an analysis of the high-pressure evolution of the W1 $H_2O$-site, occupying the pseudo-cage close to the 3-fold axis, shows a continuous decrease of the refined occupancy parameter up to 0.70 GPa ($P_4$) (Table S2). At higher pressures, the refinement of this site was not possible and an analysis of the difference-Fourier maps of the electron density revealed the absence of any unambiguous residual peak close to the former W1 position. Therefore, the W1 site was not included in the structural model in the $P$-range between 0.94 and 1.43 GPa ($P_5$-$P_7$).

### 4.3.2. *P-ramp in methanol:ethanol:water mixture*

The *V-P* patterns of the 12R-channel and pseudo-cage (Figure 6a,b, Table 2) show that the two types of cavities share, at a first approximation, the same compressional behavior in *m.e.w.*. The calculated deviation from the planarity $\Delta z$ for the S4R and the

S6R[001] (Table 2) reveals that only a minor distortion affects these building units in the (001) plane, whereas the O3–O3 and O4–O4 diameters of the S4R-joint units are basically undeformed (Table 2). In addition, also the two symmetry independent S6R[$hk0$]$_{1,2}$ windows undergo only a minor deformation with increasing pressure (Figure 7), as shown by the slight increase of the $\varepsilon_1$ and $\varepsilon_2$ parameters (Table 2).

The extraframework $H_2O$ sites detected at room-$P$ ($P_0$ in DAC), can be refined up to 2.44 GPa ($P_9$), with no substantial change in their refined coordinates. Although with a given uncertainty (see the previous paragraph and section 3), the evolution of the site occupancy factors (*s.o.f.*'s, Table S2) revealed that the calculated total number of $H_2O$ molecules per unit cell defines an increasing trend with pressure (Figure 6c).

## 5. Discussion

### *5.1 AlPO$_4$-5 structural model*

As reported in the section 1, conflicting structure models of AlPO$_4$-5 are available in the literature. Several possible solutions have been proposed. Klap et al. [19], *e.g.*, proposed a splitting of the framework oxygen sites into three mutually exclusive positions, reflecting three co-existing and mutually exclusive structural microdomains with local symmetry *P*6, which give rise to the average *P6cc*-structure. Liu et al. [25] and Berlie et al. [8] proposed the existence of several rigid unit modes of distortion in the AFI-framework, which lead to a dynamical (or static in case the RUMs condense at ambient temperature) local disorder of all the framework atoms. Both the proposed solutions allow a local tilting of the tetrahedra, reducing the Al-O2-P angle from a value close to 180° to values in the range 140-150° [8,19,25]. It is worth to note that the SiO$_2$ analogue of AlPO$_4$-5, zeolite SSZ-24, was reported to show an incommensurately modulated structure [26], with a modulation vector $q \approx 0.38\mathbf{c}^*$. Interestingly, all of the three

14

crystals we have investigated in these experiments showed the same modulation already reported by Liu et al. [26] for the $SiO_2$-analogue SSZ-24. Figure 3 shows the satellites diffraction spots, with the modulation vector $q \approx 0.37c^*$. Unfortunately, the low intensity [$I \leq 3$ sig($I$)] of the satellites diffraction spots did not allow the refinement of the incommensurate structure. Nevertheless, to the best of our knowledge, this is the first experimental evidence of an incommensurately modulated structure in crystals of the zeolite $AlPO_4$-5. In addition, the observed orientation and magnitude of the modulation vector are similar to those reported for the isotypic zeolite SSZ-24 [26], so that we can expect the same structural origin. According to Liu et al. [26], the modulation reflects the condensation of a few specific rigid unit modes involving a tilting of the tetrahedra in the (001) plane and, therefore, the closure of the P-O2-Al angle. As already pointed out by Berlie et al. [8], the presence of a dynamic or [modulated] static local disorder would induce, as a direct consequence, anomalously large anisotropic displacement parameters of the framework sites, if the structure is refined in the average *P6cc* model. This has been found also in our structure refinement based on the data collected with the crystal in air, showing the same features already reported by Klap et al. [19]. The O1, O3 and O4 sites (*i.e.* the vertices of the triangular bases of the (Al,P)$O_4$ tetrahedra) show prolate *adp*s more or less elongated along [001], whereas the O2 site (*i.e.* the hinge between the upward $AlO_4$ and the downward $PO_4$ tetrahedra) shows an oblate *adp* in the (001) plane (Figure 2b; Table S3). The shape and orientation of the refined oxygen displacement parameters are consistent with a static disorder induced by a modulated tilting of the tetrahedra in the (001) plane, as proposed by Liu et al. [26] for zeolite SSZ-24.

A further open question about the $AlPO_4$-5 structure concerns the extraframework $H_2O$ molecules. Zeolite $AlPO_4$-5 is not hydrophobic, as several experimental data (*e.g.*

15

[44–46,51]) showed that a steep adsorption of $H_2O$ molecules occurs at partial pressures of water higher than 0.3, up to 18 molecules per unit cell [46]. The structural distribution of the adsorbed $H_2O$ molecules has been studied by experimental data [46] and theoretical modeling [45,52–53]. The proposed models are characterized by $H_2O$ molecules occupying the 12R-channel and giving rise to a double-helix configuration similar to that of the hexagonal ice [46,53], governed by H-bond connections between $H_2O$ molecules. The thermogravimetric analysis performed on the previously calcined sample of this study leads to a total amount of 18.24 $H_2O$ molecules per unit cell, which demonstrates that the calcined $AlPO_4$-5 crystals likely adsorbed $H_2O$ molecules from the atmosphere after the calcination. However, the location of the $H_2O$ sites based on the diffraction data collected with the crystal in air was not straightforward. As reported in section 3, five $H_2O$ oxygen sites were assigned to diffused residual peaks in the difference-Fourier maps of the electron density (Table S2). The refined occupancies lead to a total amount of 6.4(4) molecules per unit cell, which significantly underestimate the $H_2O$ content if compared to that derived from the TG-analysis. However, this is not surprising if we consider that: 1) the refined occupancies are biased by the constrained displacement parameters and 2) a dynamical and/or static disorder should likely be considered, as suggested by the difference-Fourier maps of electron density pertaining to the extraframework population and by the possible modulated disorder of the framework. More in general, the refined structure model does not prevent the presence of clusters of H-bonded $H_2O$ molecules into the 12R-channel, as reported by Floquet et al. [46] and Demontis et al. [53]. In addition, the presence of partially occupied $H_2O$ sites in the pseudo-cages, located near the 3-fold axis centering the S6R[001], is also suggested by the structure refinement. Although the number and position of the $H_2O$ sites in the other two crystals used for the high-$P$ ramps was found

16

to be slightly different, their structural configuration is substantially analogous to that described above for the crystal collected in air.

### 5.2 High-pressure behavior of AlPO$_4$-5 and P-induced intrusion of m.e.w. molecules

Due to the non-penetrating nature of the $P$-transmitting fluid, the experimental data of the silicone oil $P$-ramp allow the description of the intrinsic elasticity of zeolite AlPO$_4$-5. The refined elastic parameters reported in Table 3 suggest that AlPO$_4$-5 is one of the softest zeolites reported so far, being its bulk modulus at ambient conditions ($K_{V0}$ = $1/\beta_V$) only 13.2(11) GPa ($\beta_V$ = 0.076(6) GPa$^{-1}$), even though a stiffening occurs with increasing pressure [$K_V'$ = $\partial K_V/\partial P$ = 5.1(14)], resulting even softer than the pure-SiO$_2$ zeolite silicalite [54]. The largest compressibility is observed along the **c**-crystallographic axis, *i.e.* along the large channels direction (Figure 1a). The refined elastic anisotropy ($K_a$:$K_c$) is found to be 1.6 at room-$P$, but tends to decrease with increasing pressure (Table 3). The bulk compressibility of zeolite AlPO$_4$-5, when compressed in *m.e.w.*, is unambiguously lower if compared to that in silicone oil, as shown in Figure 5a and by the refined elastic parameters reported in Table 3. It is interesting to note that, even though the decrease in compressibility affects both crystallographic directions (Table 3), the largest differences are observed along the **c**-axis, which is the most compressible direction in silicone oil and the less compressible one in *m.e.w* (Figure 5d). In addition, between $P_0$ and $P_1$ (0.18 GPa), a clear expansion of the *c* unit-cell parameter is observed (Figure 5d; Table 1). These data suggest the $P$-induced intrusion of the fluid molecules into the structural micropores of zeolite AlPO$_4$-5, in particular at pressures lower than 0.18 GPa ($P_1$). Due to the technical limitation related to the structure refinement (see the previous section), a direct location (or refinement) of the intruded molecules is not straightforward. No additional peaks were unambiguously found in the difference-Fourier maps of electron density. However, if

the total number of molecules per unit cell is calculated from the refined occupancies of the $H_2O$-oxygen sites at any pressure-point, a clear increasing trend is shown (Figure 6c). In addition, indirect evidences are provided by the different structural deformations underwent by $AlPO_4$-5, when compressed in the two different fluids. In fact, the significant bulk compression in silicone oil is accommodated by a strong deformation and compression of the secondary building units, especially the $S6R[hk0]_{1,2}$ windows and the S4R-joint units (Figure 7; Table 2). On the contrary, the same units are basically undistorted when compressed in *m.e.w.* (Figure 7; Table 2) and even the *P*-induced deviation from the planarity in the (001) plane ($\Delta z$) of the S6R[001] and 4-rings is less pronounced, with respect to the compression in silicone oil (Table 2). These data support the intrusion of the fluid molecules, which act as fillers preventing the *P*-induced tilting of the framework tetrahedra, and thus the deformation of specific building units, with a resulting lower compressibility of the $AlPO_4$-5 zeolite. In particular, as reported above, the most affected secondary building units are the $S6R[hk0]_{1,2}$ windows and the 4-rings, which are main components of the pseudo-cages that link the large 12R-channels (Figures 1a, 2a,c). Figure 6b shows a drastic difference in the H*P*-behavior of the modeled pseudo-cage volume: this structural cavity shows a higher compressibility in silicone oil than in *m.e.w.*, suggesting that at least a fraction of the *P*-intruded molecules are likely located in the pseudo-cage, where they act as fillers. The largest free diameter, controlled by O2–O2 (Figure 7), is ca. 3.3 and 2.8 Å (with no significant change with pressure) in the two $S6R[hk0]_{1,2}$ windows, suggesting that only $H_2O$ molecules can have access to these structural voids. On the contrary, the largest free diameter of the 12R-channels (ca. 7.4 to 6.8 Å in the range $P_0$-$P_9$) would allow the *P*-induced intrusion of either water, methanol or ethanol molecules (kinetic diameters are reported in section 2).

The behavior of the pseudo-cages in silicone oil deserves further consideration. In fact:

1) the *V-P* pattern (Figure 6b) shows an anomalous increase in compressibility with pressure and 2) the W1 site occupancy apparently decreases up to 0.70 GPa ($P_4$, Table S2). Interestingly, in the range 0.94–1.43 GPa ($P_5$-$P_7$), the refinement of the W1 site was not possible and no peaks in the difference-Fourier maps of the electron density was found at positions close to its former location. These data might suggest a *P*-induced migration of $H_2O$ molecules from the highly compressed pseudo-cages to the larger 12R-channels (*i.e.* a *P*-induced extrusion of $H_2O$ from a structural cavity to another). However, a *P*-induced migration of extraframework $H_2O$ molecules among different structural cavities was not, to the best of our knowledge, reported in the literature and we cannot exclude an artifact due to the worsening quality of the intensity data at increasing pressure.

Overall, the comparative compressional behavior of $AlPO_4$-5 in silicone oil and *m.e.w.* is a further evidence that pressure can be used for the incorporation and hyper-confinement of molecules in this zeolite, as previously reported in the literature [17,28]. In this respect, it is worth to compare the high-pressure behavior of a single crystal of $AlPO_4$-5 compressed in *m.e.w.* (this study) with that of a polycrystalline sample compressed in the same fluid [28]. Figure 5b shows that the polycrystalline sample shows a significantly lower compressibility, as also confirmed by the reported bulk modulus of 50.5(7) GPa [28], with respect to 22.2(9) GPa in this study. The lack of structure refinements from the powder data prevent a comparative structural analysis in order to explain the different elastic behavior. However, it is highly likely that the origin for the reported different elasticity would be due to a more pronounced intrusion of fluid molecules into the structural micropores of the polycrystalline $AlPO_4$-5, likely for the higher surface/volume ratio, with respect to a single crystal. In addition, in a single

crystal the presence of local defects and/or occlusions of the structural voids can hinder the intracrystalline diffusion of the intruded molecules. This effect, that was already reported in previous studies of our research group on zeolites at high pressure (e.g. [29–30]), points out that the particle size of the zeolite samples can strongly influence the magnitude of the H$P$-intrusion of fluid molecules in the structural voids of microporous materials.

## 6. Conclusions

In this study we have investigated the high-pressure behavior of the zeolite AlPO$_4$-5 by *in situ* single-crystal synchrotron X-ray diffraction, using silicone oil and the (16:3:1) methanol:ethanol:water mixture as $P$-transmitting fluids. Interestingly, all the single crystals used for this study showed a diffraction pattern with an incommensurate modulation analogous to that reported for the isotypic zeolite SSZ-24 [26]. The elastic parameters based on the compression experiment in silicone oil show that AlPO$_4$-5 is one of the softest zeolites reported so far, with a refined bulk compressibility at ambient conditions of $\beta_V$ = 0.076(6) GPa$^{-1}$. The compressibility in *m.e.w.* is significantly lower than that observed in the non-penetrating silicone oil, suggesting the $P$-induced intrusion of the fluid molecules into the structural micropores likely at pressures < 0.18 GPa. An indirect evidence for the molecules intrusion is provided by the different magnitude of specific mechanisms of structural deformation, when the studied zeolite is compressed in the two different fluids. In particular, a lower compressibility and a lower degree of distortion are observed for the building units related to the pseudo-cages linking neighboring channels, suggesting that the intrusion of H$_2$O molecules probably affects (at least partially) these voids. If only H$_2$O can be intruded into the pseudo-

cages, due to steric hindrances controlled by the S6R[$hk0$]$_{1,2}$ windows, either methanol and ethanol can, in principle, be intruded into the large 12R-channels, though a clear picture in this respect is still missing. Interestingly, the compressibility observed for our single crystal of AlPO$_4$-5 in *m.e.w.* is significantly higher than that observed for a polycrystalline sample of the same zeolite compressed in the same *P*-fluid [28]. This finding suggests that the sample size somehow controls the magnitude of the *P*-induced intrusion process.

Overall, this study confirms the suitability of zeolite AlPO$_4$-5 as a host material for the *P*-induced intrusion of fluid molecules. Although a thorough quantitative and structural characterization of the intrusion process was not possible in this and in the previous studies [17,28], the results here reported suggest that the zeolite AlPO$_4$-5 is a promising material for the penetration, at high-pressure, of a relatively high number of molecules per unit cell. In this respect, it could be worth to investigate, among the potential applications of this versatile compound, its use in systems for the mechanical energy storage/dissipation [55–57].

### 7. Acknowledgements

## 8.  References

[1] S.T. Wilson, B.M. Lok, C.A. Messina, T.R. Cannan, E.M. Flanigen, J. Am. Chem. Soc., 104 (1982) 1146–1147.

[2] E.M. Flanigen, B.M. Lok, R.L. Patton, S.T. Wilson, Pure Appl. Chem., 58 (1988) 1351–1358.

[3] J. Yu, R. Xu, Acc. Chem. Res., 36 (2003) 481–490.

[4] J.M. Bennet, J.P. Cohen, E.M. Flanigen, J.J. Pluth, J.V. Smith, in: G.D. Stucky, F.G. Dwyer (Eds.), Intrazeolite Chemistry, ACS Sym. Ser., 218, American Chemical Society, Washington DC, 1983, pp. 109–118.

[5] C. Baerlocher, L.B. McCusker, D.H. Olson, Atlas of Zeolite Framework Types, sixth ed., Elsevier, Amsterdam, 2007.

[6] Y. Shi, G. Liu, L. Wang, X. Zhang, Micropor. Mesopor. Mat., 193 (2014) 1–6.

[7] X. Zhao, J. Zhao, J. Wen, A. Li, G. Li, X. Wang, Micropor. Mesopor. Mat., 213 (2015) 192–196.

[8] A. Berlie, G.J. Kearley, Y. Liu, D. Yu, R.A. Mole, C.D. Ling, R.L. Withers, Phys. Chem. Chem. Phys., 17 (2015) 21547–21554.

[9] D. Liu, B. Zhang, X. Liu, J. Li, Catal. Sci. Technol., 5 (2015) 3394–3402.

[10] Y. Chen, Y. Zhang, D. Li, F. Gao, C. Feng, S. Wen, S. Ruan, Sensor. Actuat. B-Chem., 212 (2015) 242–247.

[11] W. Yang, W. Sun, S. Zhao, X. Yin, Micropor. Mesopor. Mat., 219 (2016) 87–92.

[12] Z.K. Tang, H.D. Sun, J. Wang, J. Chen, G. Li, Appl. Phys. Lett., 16 (1998) 2287–2289.

[13] Z.M. Li, Z.K. Tang, H.J. Liu, N. Wang, C.T. Chan, R. Saito, S. Okada, G.D. Li, J.S. Chen, N. Nagasawa, S. Tsuda, Phys. Rev. Lett., 87 (2001) 127401.

[14] Ö. Weiß, J. Loerke, U. Wüstefeld, F. Marlow, F. Schüth, J. Solid State Chem., 167 (2002) 302–309.

[15] H. Lim, H. Cheong, S. Choi, Y.N. Choi, J.S. Lee, J. Korean Phys. Soc., 58 (2011) 1035–1038.

[16] M. Yao, T. Wang, Z. Yao, D. Duan, S. Chen, Z. Liu, R. Liu, S. Lu, Y. Yuan, B. Zou, T. Cui, B. Liu, J. Phys. Chem. C, 117 (2013) 25052–25058.

[17] H. Lv, M. Yao, Q. Li, R. Liu, B. Liu, S. Lu, L. Jiang, W. Cui, Z. Liu, J. Liu, Z. Chen, B. Zou, T. Cui, B. Liu, J. Appl. Phys., 111 (2012) 112615.

[18] P. Bordat, J. Kirstein, P. Labéguerie, M. Merawa, R. Brown, J. Phys. Chem. C, 111 (2007) 10972–10981.

[19] G.J. Klap, H. van Koningsveld, H. Graafsma, A.M.M. Shreurs, Micropor. Mesopor. Mat., 38 (2000) 403–412.

[20] A.J. Mora, A.N. Fitch, M. Cole, R. Goyal, R.H. Jones, H. Jobic, S.W. Carr, J. Mater. Chem., 6 (1996) 1831–1835.

[21] T. Ikeda, K. Miyazawa, F. Izumi, Q. Huang, A. Santoro, Phys. Chem. Solids, 60 (1999) 1531–1353.

[22] N. Ohnishi, S. Qiu, O. Terasaki, T. Kajitani, K. Hiraka, Micropor. Mater., 2 (1992) 73–74.

[23] E. de Vos Burchart, H. van Bekkum, B. van de Graaf, E.C.T. Vogt, J. Chem. Soc., Faraday Trans., 88 (1992) 2761–2769.

[24] A.R. Ruiz-Salvador, G. Sastre, D.W. Lewis, R.A. Catlow, J. Mater. Chem., 6 (1996) 1837–1842.

[25] Y. Liu, R.L. Withers, L. Norén, Solid State Sci., 5 (2003) 427–434.

[26] Z. Liu, N. Fuita, O. Terasaki, T. Ohsuna, K. Hiraga, M.A. Camblor, M-J. Diaz-Cabañas, A.K. Cheetham, Chem. Eur. J., 8 (2002) 4549–4556.

[27] G.D. Gatta, Y. Lee, Mineral. Mag., 78 (2014) 267–291.

[28] T. Kim, Y. Lee, Y-N. Jang, J. Shin, S.B. Hong, Micropor. Mesopor. Mat., 169 (2013) 42–46.

[29] P. Lotti, R. Arletti, G.D. Gatta, S. Quartieri, G. Vezzalini, M. Merlini, V. Dmitriev, M. Hanfland, Micropor. Mesopor. Mat., 218 (2015) 42–54.

[30] P. Lotti, G.D. Gatta, M. Merlini, H-P. Liermann, Z. Kristallogr., 230 (2015) 201–211.

[31] R. Arletti, G. Vezzalini, S. Quartieri, F. Di Renzo, V. Dmitriev, Micropor. Mesopor. Mat., 191 (2014) 27–37.

[32] R. Arletti, L. Leardini, G. Vezzalini, S. Quartieri, L. Gigli, M. Santoro, J. Haines, J. Rouquette, L. Konczewicz, Phys. Chem. Chem. Phys., 17 (2015) 24262–24274.

[33] G.D. Gatta, K.S. Scheidl, T. Pippinger, R. Skála, Y. Lee, R. Miletich, Micropor. Mesopor. Mat., 206 (2015) 34–41.

[34] L. Gigli, R. Arletti, G. Tabacchi, E. Fois, J.G. Vitillo, G. Martra, G. Agostini, S. Quartieri, G. Vezzalini, J. Phys. Chem. C, 118 (2014) 15732–15743.

[35] D. Li, J. Yao, H. Wang, Prog. Nat. Sci. Mater. Int., 22 (2012) 684–692.

[36] M. Merlini, M. Hanfland, High Pressure Res., 33 (2013) 511–522.

[37] R.J. Angel, M. Bujak, J. Zhao, G.D. Gatta, S.J. Jacobsen, J. Appl. Crystallogr., 40 (2007) 26-32.

[38] H.K. Mao, J. Xu, P.M. Bell, J. Geophys. Res., 91 (1986) 4673–4676.

[39] J.C. Chervin, B. Canny, M. Mancinelli, High Pressure Res., 21 (2001) 302–314.

[40] T.J.B. Holland,  S.A.T. Redfern, Mineral. Mag., 61 (1997) 65–77.

[41] Agilent, Chrysalis RED, Agilent Technologies Ltd, Yarnton, 2012.

[42] V. Petricek, M. Dusak, L. Palatinus, Z. Kristallogr., 229 (2014) 345–352.

[43] L. Palatinus, G. Chapuis, J. Appl. Crystallogr., 41 (2007) 786–790.

[44] P.B. Malla, S. Komarneni, Zeolites, 15 (1995) 324–332.

[45] B.L. Newalkar, R.V. Jasra, V. Kamath, S.G.T. Bhat, Micropor. Mesopor. Mat., 20 (1998) 129–137.

[46] N. Floquet, J.P. Coulomb, N. Dufau, G. Andre, J. Phys. Chem. B, 108 (2004) 13107–13115.

[47] R.J. Angel, in: R.M. Hazen, R.T. Downs (Eds.), High-Temperature and High-Pressure Crystal Chemistry,  Rev. Mineral. Geochem., 41, Mineralogical Society of America and Geochemical Society, Washington DC, 2000, pp. 35–60.

[48] R.J. Angel, M. Alvaro, J. Gonzalez-Platas, Z. Kristallogr., 229 (2014) 405–419.

[49] G.D. Gatta, Z. Kristallogr., 223 (2008) 160–170.

[50] G.D. Gatta, Micropor. Mesopor. Mat., 128 (2010) 78–84.

[51] K. Tsutsumi, K. Mizoe, K. Chubaci, Colloid Polym. Sci., 277 (1999) 83–88.

[52] R.S. Pillai, R.V. Jasra, Langmuir, 26 (2010) 1755–1764.

[53] P. Demontis, J. Gulín-González, G.B. Suffritti, J. Phys. Chem. C, 116 (2012) 11100–11109.

[54] G. Vezzalini, R. Arletti, S. Quartieri, Acta Cryst., B70, (2014) 444–451.

[55] V. Eroshenko, R.C. Regis, M. Soulard, J. Patarin, J. Am. Chem. Soc., 123 (2001) 8129–8130.

[56] M. Soulard, J. Patarin, V. Eroshenko, R. Regis, Stud. Surf. Sci. Catal., 154 (2004) 1830–1837.

[57] A. Ryzhikov, I. Khay, H. Nouali, T.J. Daou, J. Patarin, Micropor. Mesopor. Mat., 221 (2016) 1–7.

**Table 1**: Unit-cell parameters of the zeolite AlPO$_4$-5 based on the experiment performed with the crystal in air and on the high-$P$ experiments in silicone oil and in *m.e.w.*

| Experiment | $P$ | (GPa) | $a$ (Å) | $c$ (Å) | $V$ (Å$^3$) |
|---|---|---|---|---|---|
| AIR | | 0.0001 | 13.7175(12) | 8.4350(8) | 1374.6(2) |
| Silicone oil | $P_1$ | 0.25 | 13.6921(8) | 8.326(3) | 1351.8(4) |
| " | $P_2$ | 0.39 | 13.6470(8) | 8.302(3) | 1339.0(4) |
| " | $P_3$ | 0.54 | 13.6031(8) | 8.264(3) | 1324.4(4) |
| " | $P_4$ | 0.70 | 13.5723(8) | 8.228(3) | 1312.5(4) |
| " | $P_5$ | 0.94 | 13.5122(8) | 8.185(3) | 1294.1(4) |
| " | $P_6$ | 1.17 | 13.4663(7) | 8.152(3) | 1280.3(4) |
| " | $P_7$ | 1.43 | 13.3984(7) | 8.108(2) | 1260.6(3) |
| " | $P_8$ | 1.65 | 13.3568(10) | 8.080(3) | 1248.4(5) |
| *m.e.w.* | $P_0$ | 0.0001* | 13,7179(10) | 8.4191(5) | 1372.06(17) |
| " | $P_1$ | 0.18 | 13.6747(15) | 8.4316(6) | 1365.4(2) |
| " | $P_2$ | 0.36 | 13.6472(15) | 8.4175(6) | 1357.7(3) |
| " | $P_3$ | 0.58 | 13.6095(14) | 8.3996(6) | 1347.3(2) |
| " | $P_4$ | 0.77 | 13.5656(14) | 8.3823(6) | 1335.9(3) |
| " | $P_5$ | 1.02 | 13.5264(14) | 8.3654(6) | 1325.5(2) |
| " | $P_6$ | 1.36 | 13.4498(14) | 8.3307(6) | 1305.1(2) |
| " | $P_7$ | 1.65 | 13.4068(13) | 8.3126(6) | 1293.9(2) |
| " | $P_8$ | 2.05 | 13.3258(11) | 8.2754(7) | 1272.64(18) |
| " | $P_9$ | 2.44 | 13.2539(11) | 8.2459(6) | 1254.46(19) |
| " | $P_{10}$ | 2.94 | 13.1668(11) | 8.2068(5) | 1232.15(18) |
| | $P_{11}$ | 3.77 | 13.0366(14) | 8.1474(6) | 1199.2(2) |
| | $P_{12}$ | 4.77 | 12.8980(14) | 8.0776(7) | 1163.7(2) |
| | $P_{13}$ | 5.48 | 12.8084(18) | 8.0399(12) | 1142.3(3) |
| | $P_{14}$ | 6.51 | 12.717(2) | 7.9967(14) | 1120.0(3) |
| | $P_{15d}$ | 0.82 | 13.2975(14) | 8.3213(6) | 1274.3(2) |
| | $P_{16d}$ | 0.75 | 13.3356(14) | 8.3412(6) | 1284.6(2) |

*with the crystal in the DAC without the $P$-transmitting fluid; d = in decompression

**Table 2.** High-pressure evolution of: 12R-channel and pseudo-cages volume (see section 4.3.1 for further details), relevant interatomic distances, S4R- and S6R[001]-deviation from the planarity in the (001) plane and distortion parameters of the S6R[$hk0$]$_{1,2}$ windows [$\varepsilon = d1/d2 =$ (O1–O3/O1–O3)$_1$ and (O1–O4/O1–O4)$_2$, see Figure 2a,c].

| Exp. | $P$ | (GPa) | $V_{ch}$ (Å³) | $V_{cg}$ (Å³) | O1–O1$_{ch}$ (Å) | O3–O3$_{ch}$ (Å) | O3-O3$_{4R}$ (Å) | O4–O4$_{4R}$ (Å) | $\Delta z_{4R}$ (Å) | $\Delta z_{6R[001]}$ (Å) | $\varepsilon_{6R[hk0]1}$ | $\varepsilon_{6R[hk0]2}$ |
|---|---|---|---|---|---|---|---|---|---|---|---|---|
| AIR | | 0.0001 | 671(3) | 358.5(9) | 10.112(12) | 10.015(8) | 3.702(8) | 3.52(2) | 0.1080(7) | 0.155(1) | 1.056(9) | 1.008(6) |
| Sil. oil | $P_1$ | 0.25 | 652(4) | 360(1) | 10.02(2) | 9.951(10) | 3.750(11) | 3.64(2) | 0.0416(7) | 0.225(5) | 1.11(2) | 1.08(2) |
| " | $P_2$ | 0.39 | 645(4) | 357.0(9) | 9.96(2) | 9.930(11) | 3.729(11) | 3.639(19) | 0.174(3) | 0.174(3) | 1.09(2) | 1.01(2) |
| " | $P_3$ | 0.54 | 640(4) | 351(1) | 9.94(2) | 9.926(11) | 3.696(11) | 3.59(2) | 0.174(4) | 0.306(7) | 1.15(3) | 1.07(2) |
| " | $P_4$ | 0.70 | 637(4) | 344(1) | 9.99(2) | 9.864(12) | 3.727(13) | 3.53(2) | 0.115(6) | 0.44(2) | 1.24(7) | 1.17(6) |
| " | $P_5$ | 0.94 | 626(6) | 334.6(9) | 9.92(3) | 9.823(15) | 3.649(16) | 3.45(2) | 0.090(1) | 0.434(6) | 1.25(2) | 1.18(2) |
| " | $P_6$ | 1.17 | 622(6) | 322(1) | 9.82(3) | 9.897(19) | 3.59(2) | 3.31(3) | 0.302(8) | 0.661(14) | 1.39(4) | 1.20(4) |
| " | $P_7$ | 1.43 | 617(6) | 305(1) | 9.71(3) | 9.984(16) | 3.516(17) | 3.05(3) | 0.284(8) | 0.738(19) | 1.41(4) | 1.32(4) |
| *m.e.w.* | $P_0$ | 0.0001 | 632(5) | 369(1) | 9.85(2) | 9.711(17) | 4.016(18) | 3.70(3) | 0.008420(7) | 0.2484(2) | 1.103(9) | 1.096(9) |
| " | $P_1$ | 0.18 | 631(5) | 371(1) | 9.84(2) | 9.682(19) | 4.00(2) | 3.76(2) | 0.06914(5) | 0.3221(2) | 1.121(9) | 1.096(9) |
| " | $P_2$ | 0.36 | 629(5) | 367(1) | 9.86(2) | 9.65(2) | 4.00(2) | 3.70(2) | 0.05892(5) | 0.3207(3) | 1.126(9) | 1.103(9) |
| " | $P_3$ | 0.58 | 619(5) | 365(1) | 9.74(2) | 9.643(18) | 3.974(18) | 3.71(2) | 0.10332(8) | 0.3351(3) | 1.130(9) | 1.085(9) |
| " | $P_4$ | 0.77 | 612(5) | 361(1) | 9.67(2) | 9.614(18) | 3.961(19) | 3.69(3) | 0.08634(7) | 0.3688(3) | 1.15(1) | 1.108(9) |

| | | | | | | | | | | | |
|---|---|---|---|---|---|---|---|---|---|---|---|
| " | $P_5$ | 1.02 | 606(5) | 362(1) | 9.70(2) | 9.51(2) | 4.02(2) | 3.74(3) | 0.08365(7) | 0.3430(3) | 1.15(1) | 1.090(9) |
| " | $P_6$ | 1.36 | 613(5) | 350(1) | 9.74(2) | 9.622(19) | 3.832(19) | 3.62(3) | 0.06665(6) | 0.3416(3) | 1.16(1) | 1.094(9) |
| " | $P_7$ | 1.65 | 600(5) | 345(1) | 9.76(2) | 9.41(2) | 4.01(2) | 3.57(3) | 0.09310(8) | 0.3741(3) | 1.16(1) | 1.077(9) |
| " | $P_8$ | 2.05 | 571(5) | 341(1) | 9.51(2) | 9.24(2) | 4.11(2) | 3.58(3) | 0.05793(6) | 0.3807(4) | 1.16(1) | 1.087(9) |
| " | $P_9$ | 2.44 | 548(7) | 339(1) | 9.28(2) | 9.13(3) | 4.16(3) | 3.59(4) | 0.1897(2) | 0.1979(3) | 1.07(2) | 1.12(1) |

**Table 3.** Refined elastic parameters of AlPO$_4$-5, based on III-BM equations of state fits, with the crystal compressed in silicone oil (0.25–1.65 GPa) and in *m.e.w.* (0.18–6.51 GPa) (see section 4.2 for further details).

**Silicone oil experiment**

|  | $V_0, l_0$ (Å$^3$, Å) | $K_0$ (GPa) | $K'$ | $\beta_{V,l}$ (GPa$^{-1}$) |
|---|---|---|---|---|
| *V* | 1376(3) | 13.2(11) | 5.1(14) | 0.076(6) |
| *a* | 13.759(5) | 15.5(3) | 4* | 0.0215(4) |
| *c* | 8.369(4) | 9.6(2) | 7* | 0.0347(7) |

**(16:3:1) methanol:ethanol:water experiment**

|  | $V_0, l_0$ (Å$^3$, Å) | $K_0$ (GPa) | $K'$ | $\beta_{V,l}$ (GPa$^{-1}$) |
|---|---|---|---|---|
| *V* | 1360(2) | 22.2(9) | 3.0(3) | 0.045(2) |
| *a* | 13.734(9) | 19.7(7) | 3.0(3) | 0.0169(6) |
| *c* | 8.453(3) | 29.3(10) | 2.9(4) | 0.0114(4) |

\* fixed parameter; $K_{V0} = (1/\beta_V)_{room-P,T}$; $K_{l0} = (1/3\beta_l)_{room-P,T}$; $K' = (\partial K/\partial P)_T$

**Figure Captions**

**Figure 1**. (*A*). The AFI framework of the zeolite $AlPO_4$-5 viewed down the **c** crystallographic axis. The secondary building units and some relevant interatomic distances reported in Table 2 are shown. (*B*). The AFI framework viewed along the **b** crystallografic axis. The sheets made by upward $AlO_4$ and downward $PO_4$ tetrahedra are shown.

**Figure 2**. (*A*) A view of the two symmetry-independent 6-membered rings "windows" of tetrahedra ($S6R[hk0]_{1,2}$) defining the access between neighboring 12R-channels. A schematic view of the two symmetry-independent $S6R[hk0]_{1,2}$ "windows" is also given in (*C*). (*B*) Upward $AlO_4$ and downward $PO_4$ tetrahedra, shown with the anisotropic displacement parameters and based on the structure refinement with the crystal in air of this study (displacement probability factor: 50%).

**Figure 3**. A fraction of the reconstructed ($h1l$) * reciprocal lattice plane, based on the $P_1$ (0.25 GPa) dataset in silicone oil. The satellite diffraction spots of the incommensurately modulated structure, with modulation vector $q \approx 0.37\mathbf{c}^*$, are shown. More details are given in section 5.1. Note that the spot close to the horizontal arrow representing $\mathbf{a}^*$ belongs to the diamond diffraction pattern and is not related to the incommensurately modulated structure of zeolite $AlPO_4$-5.

**Figure 4**. TG (*solid line*) and DTG (*dashed line*) experimental patterns of the previously calcined $AlPO_4$-5 synthetic sample.

**Figure 5**. (*A*) High-pressure evolution of the normalized unit-cell volume of the zeolite $AlPO_4$-5 compressed in silicone oil and *m.e.w.* (*B*) Comparison of the experimental $V/V_0$ *vs. P* patterns of the zeolite $AlPO_4$-5 compressed in *m.e.w.*, based on *in situ* single-

crystal (round symbols, this study) and powder (diamond symbols [28]) X-ray diffraction data. ($C$ and $D$) $P$-induced evolution of the normalized unit-cell $a$ and $c$ parameters of the zeolite $AlPO_4$-5 compressed in silicone oil and *m.e.w.* The Birch-Murnaghan equations of state, fitting the experimental data (see section 4.2), are reported as solid lines in $A$, $C$ and $D$. Data related to the silicone oil experiments have been normalized to the $V_0$, $a_0$ and $c_0$ refined by the BM-EoS fits.

**Figure 6.** High-pressure evolution of the calculated volumes of ($A$) the 12R-channels and ($B$) pseudo-cage cavities. ($C$) $P$-induced evolution of the total number of extraframework $H_2O$ molecules per unit cell, deduced from the structure refinements related to the *m.e.w.* experiment.

**Figure 7.** A view of the deformation mechanisms with pressure of the $S6R[hk0]_1$ window of zeolite $AlPO_4$.

**Figure 1 - revised**
**Click here to download high resolution image**

A

S6R[hk0]₂

O3  O4

O1

O2

O2

O2

O4

O3

O1

S6R[hk0]₁

a c b

B

O3

O4

O1  P

O2

c

a

b

O3  Al

O3

O1  O4

C

S6R[hk0]₂

O4

O3  O1

O2

O2

O2

O4

O3

c

b

O1

a

S6R[hk0]₁
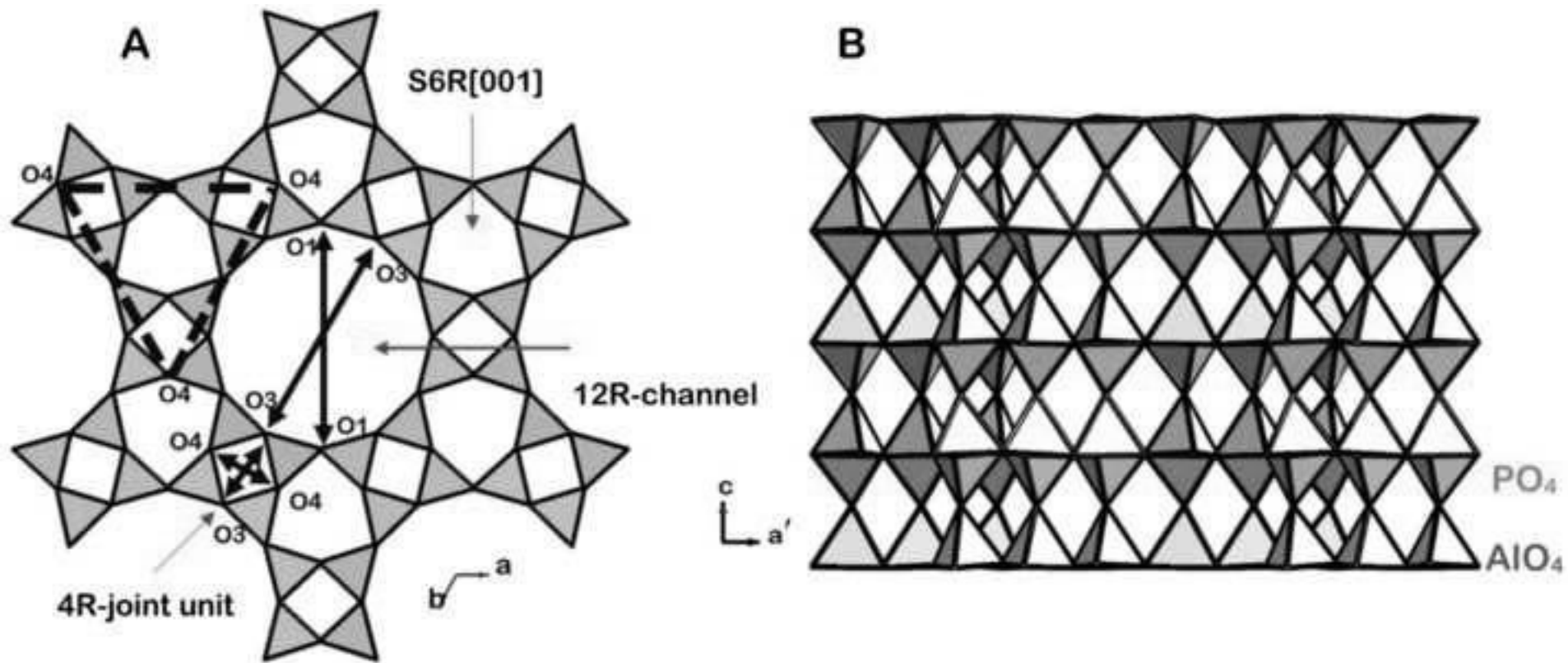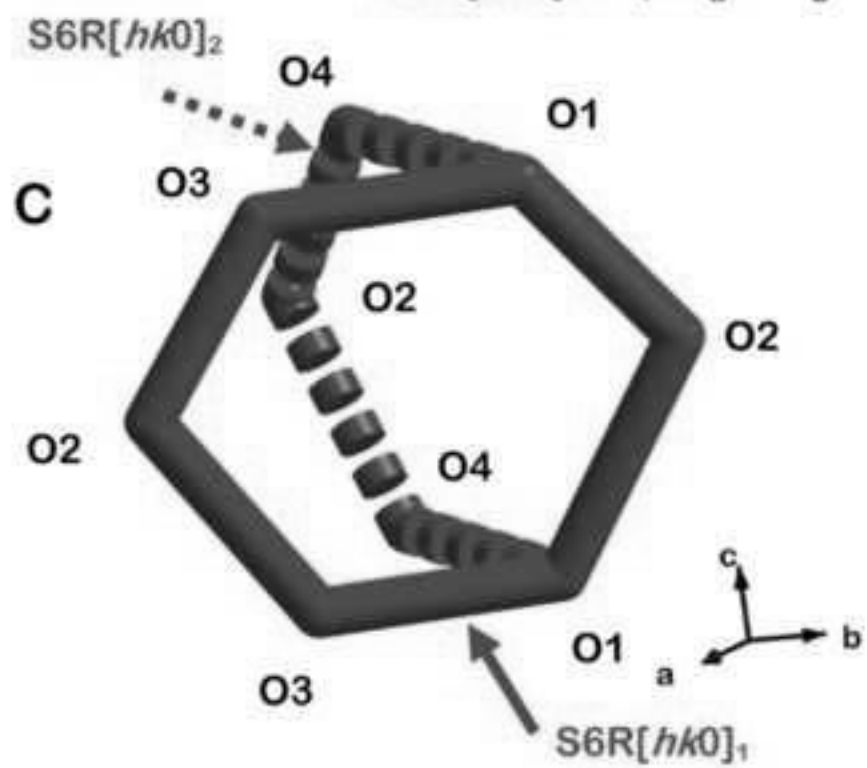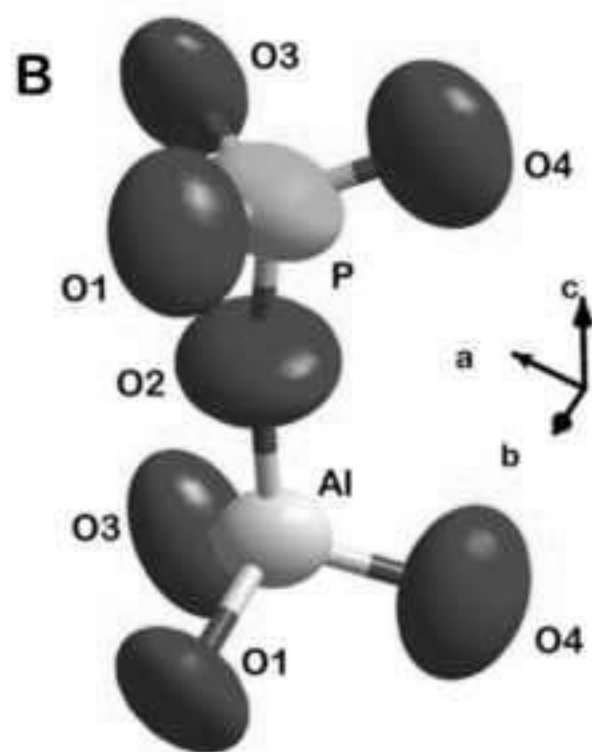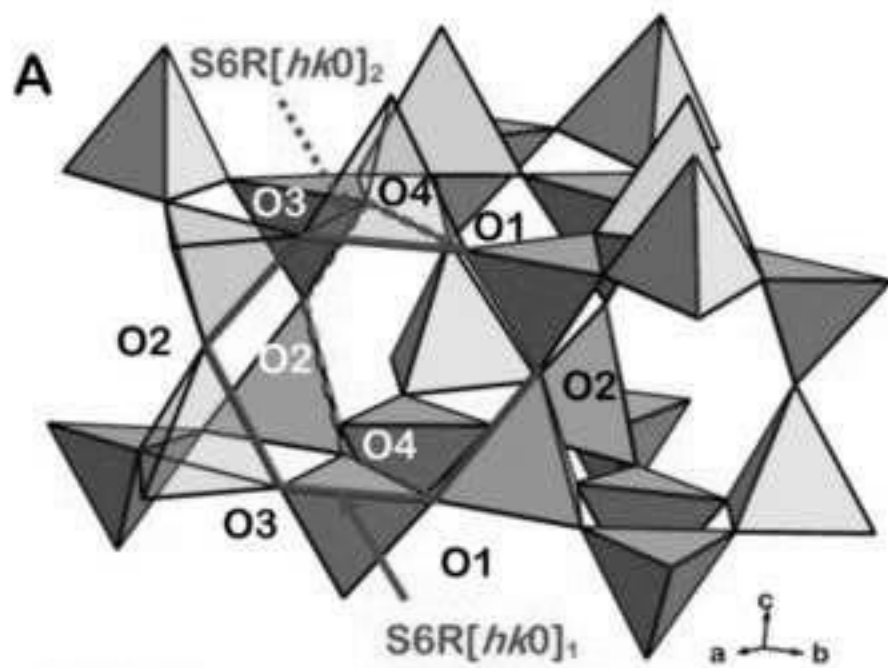
**Figure 3**
**Click here to download high resolution image**
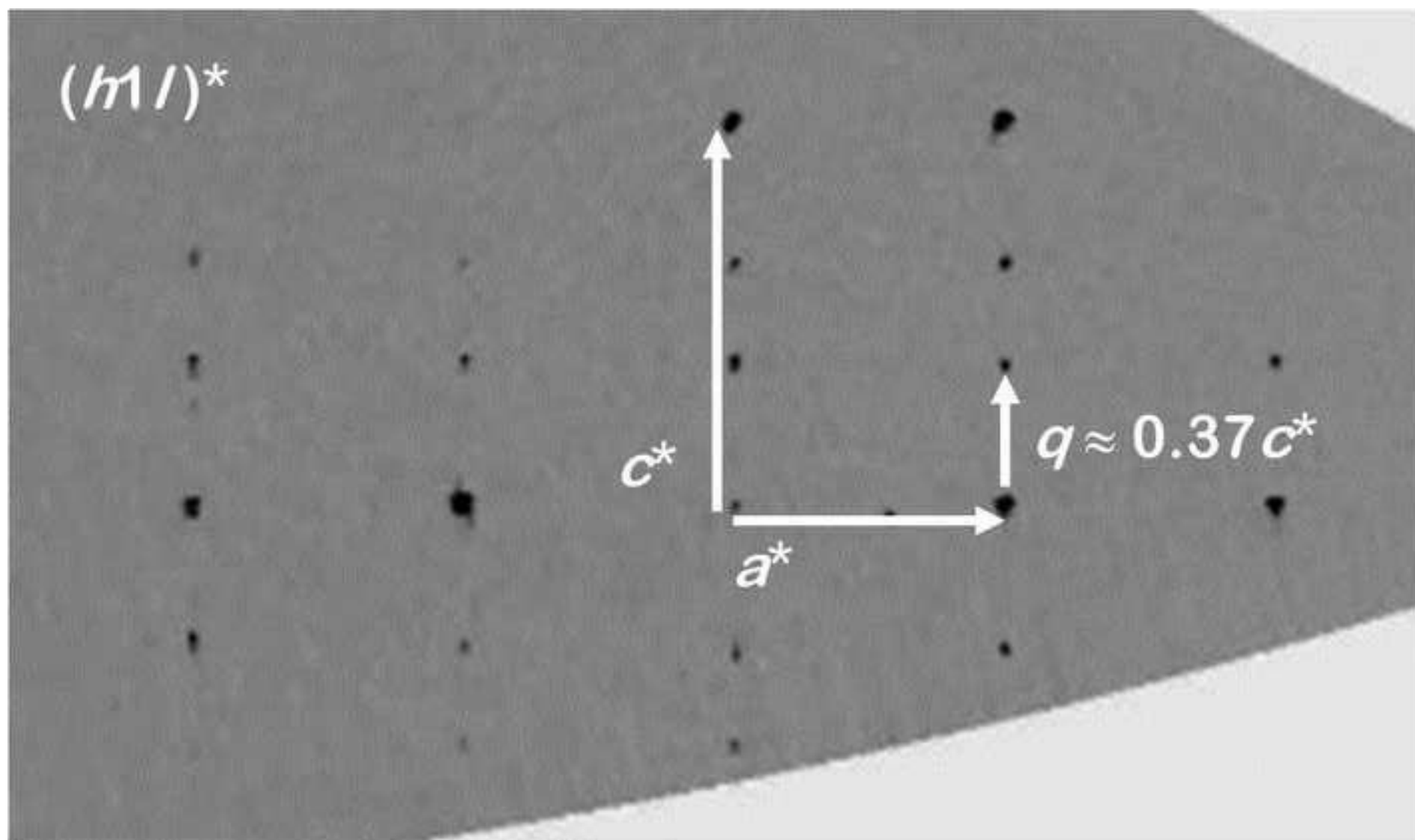
**Figure 4 - revised**
**Click here to download high resolution image**
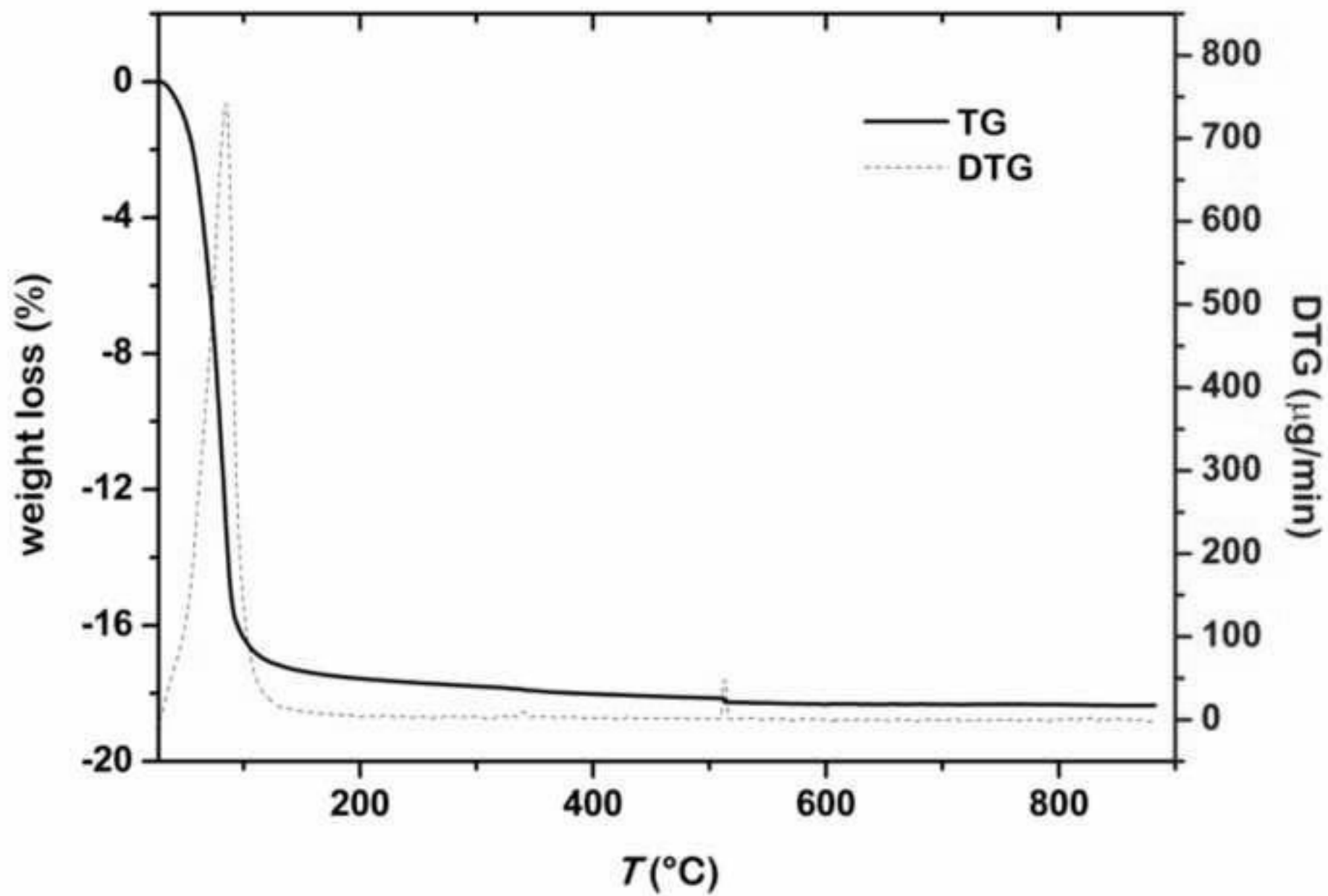
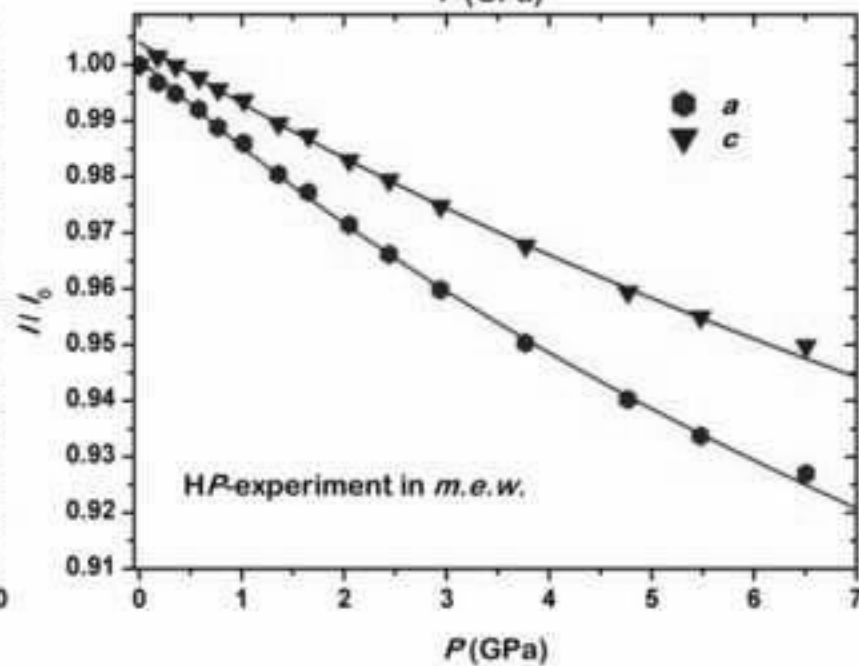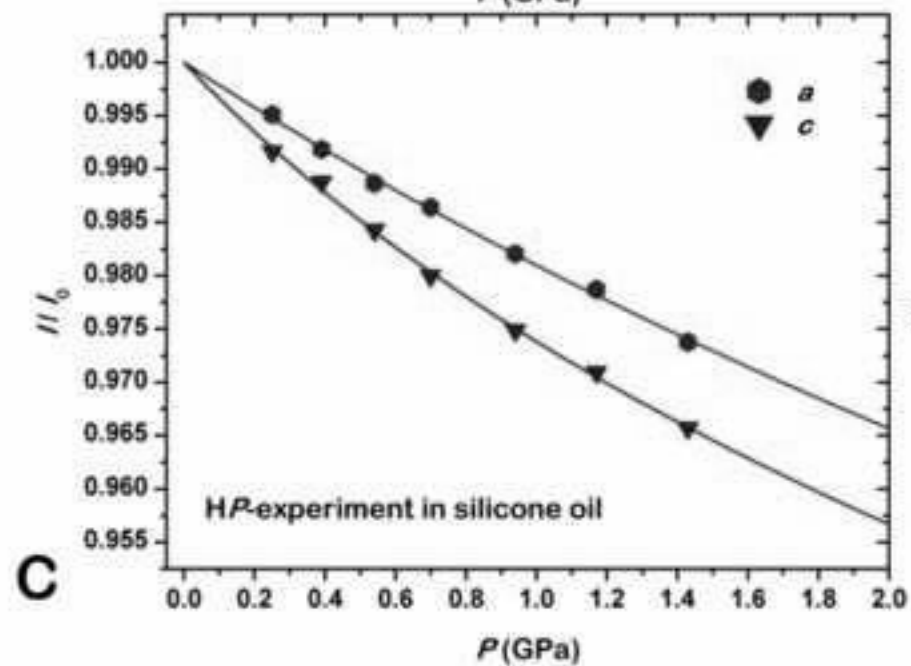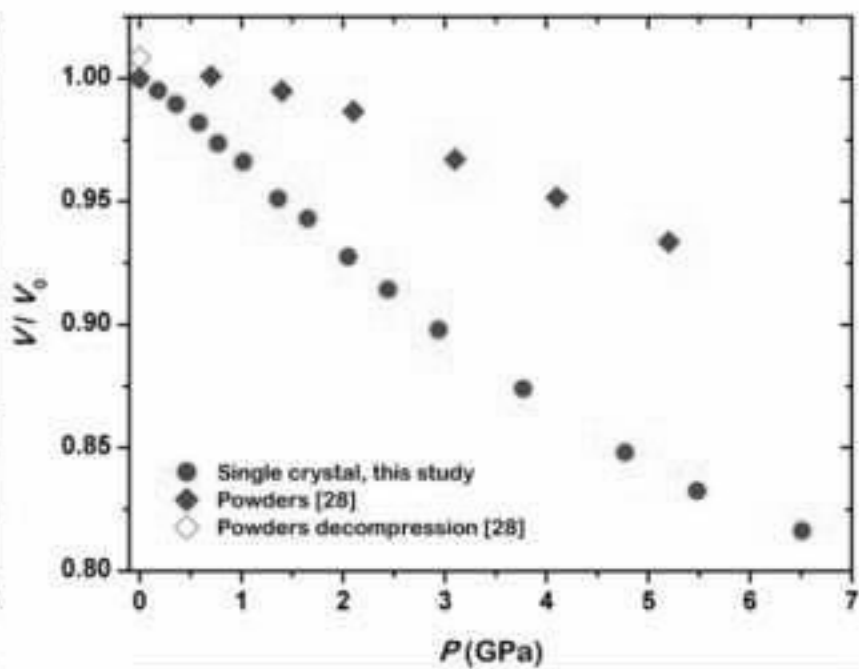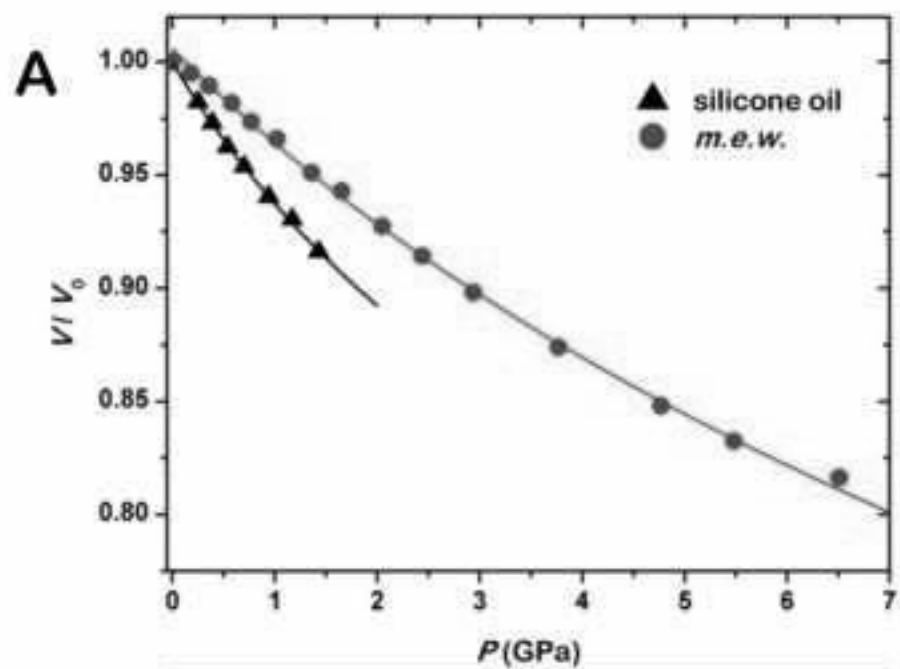**Figure 5 - revised**
**Click here to download high resolution image**

**Figure 6 - revised**
**Click here to download high resolution image**
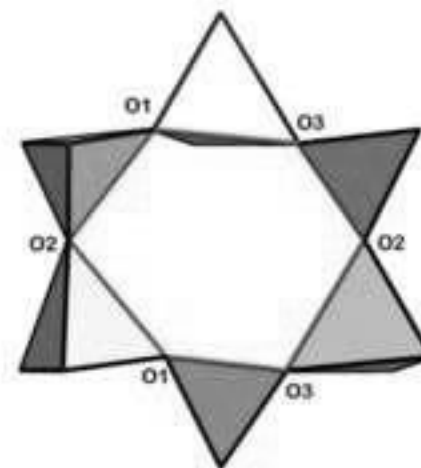
**Figure 7 - revised**
**Click here to download high resolution image**



Silicone oil experiment

0.25 GPa

1.43 GPa

m.e.w. experiment

0.0001 GPa

2.44 GPa